


Superelastic, Fatigue-Resistant, and Flame-Retardant Spongy Conductor for Human Motion Detection against a Harsh High-Temperature Condition

Zhichong Liu, Kening Wan, Tianyi Zhu, Jixin Zhu, Jingsan Xu, Chao Zhang,* and Tianxi Liu

 Cite This: *ACS Appl. Mater. Interfaces* 2021, 13, 7580–7591 Read Online

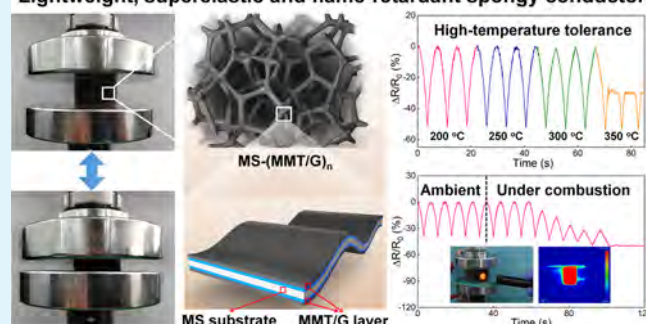
ACCESS |

 Metrics & More Article Recommendations Supporting Information

ABSTRACT: The construction of wearable piezoresistive sensors with high elasticity, large gauge factor, and excellent durability in a harsh high-temperature environment is highly desired yet challenging. Here, a lightweight, superelastic, and fatigue-resistant spongy conductor was fabricated via a sponge-constrained network assembly, during which highly conductive graphene and flame-retardant montmorillonite were alternatively deposited on a three-dimensional melamine scaffold. The as-obtained spongy conductor exhibited a highly deformation-tolerant conductivity up to 80% strain and excellent fatigue resistance of 10,000 compressive cycles at 70% strain. As a result, the spongy conductor can readily work as a piezoresistive sensor and exhibited a high gauge factor value of ~ 2.3 in a strain range of 60–80% and excellent durability under 60% strain for 10,000 cycles without sacrificing its piezoresistive performance. Additionally, the piezoresistive sensor showed great thermal stability up to 250 °C for more than 7 days and sufficient flame-retardant performance for at least 20 s. This lightweight, superelastic, and flame-retardant spongy conductor reveals tremendous potential in human motion detection against a harsh high-temperature environment.

KEYWORDS: sponge-constrained network assembly, spongy conductor, elasticity, wearable piezoresistive sensor, flame-retardant property

Lightweight, superelastic and flame-retardant spongy conductor



1. INTRODUCTION

Flexible electronics are an emerging research field of electronics by combining active electronic materials with flexible materials to obtain excellent flexibility and stretchability of devices, which have attracted intense interest in the fields of smart life, healthcare, and motion detection during the past decade.^{1–4} Wearable piezoresistive sensors with features of lightweight and high compressibility are capable of realizing real-time and rapid monitoring of physical stimuli by emulating human skin, showing high potentials in practical demands of human-machine interfaces, soft robotics, biomedicines, and so forth.^{5–17} Conductive percolation theory of conductive polymer composites has provided a theoretical basis for the development of high-performance piezoresistive sensors in recent years, mainly focusing on the innovation of new-type of conductive structures in piezoresistive sensors. The construction of the spongy structure of sensitive materials and the surface microstructure of sensitive layers are two important innovations for piezoresistive sensors.^{18–20} The piezoresistive sensing mechanism mainly depends on a reversible evolution in conductive networks, that is, the variation of electrical resistance derived from the deformation to external stimuli. Piezoresistive sensors usually exhibit advantages of high sensitivity, fast response time, simple manufacturing, and low energy con-

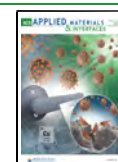
sumption. However, the lack of good ductility and high cycling stability limits their portable and wearable applications. Apart from meeting the demands in daily wearable applications,²¹ sometimes, piezoresistive sensors are also employed in harsh and high-temperature environments such as flaming, welding, and forging conditions.^{22,23} However, the state-of-the-art piezoresistive sensors, which can tolerate extremely high-temperatures, are still in their infancy.

Conductive porous sponges are regarded as alternatives for piezoresistive sensors because of their feasible preparation, low cost, and high elasticity.^{24–27} Nanocarbon materials are promising conductive nano-additives because of their low cost, diverse forms, and excellent conductivity.^{28–30} However, the wide applications of conductive polymer composites have been seriously affected by the easy-aggregation and difficult-controlled network structure of conductive nanocarbon.^{31–34}

Received: November 23, 2020

Accepted: January 27, 2021

Published: February 5, 2021



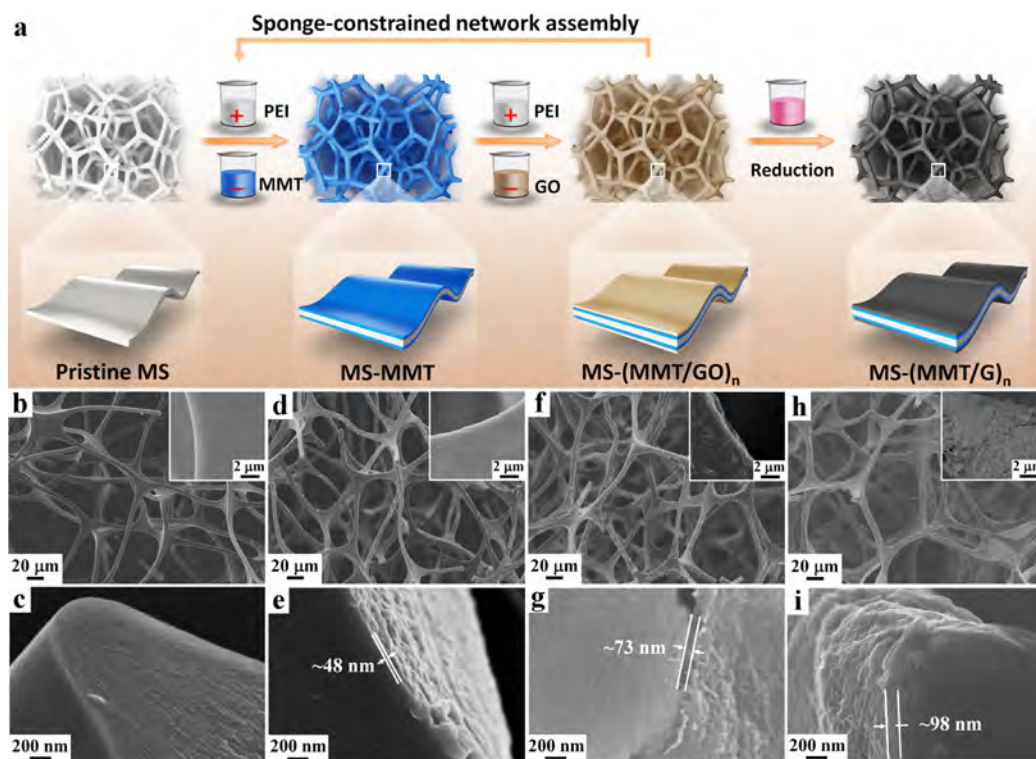


Figure 1. (a) Schematic of the preparation procedure of $\text{MS}-(\text{MMT}/\text{G})_n$ via a sponge-constrained network assembly. Surface and cross-section SEM images of $\text{MS}-(\text{MMT}/\text{G})_n$ with various numbers of deposition cycles: (b,c) pristine MS, (d,e) $\text{MS}-(\text{MMT}/\text{G})_2$, (f,g) $\text{MS}-(\text{MMT}/\text{G})_3$, and (h,i) $\text{MS}-(\text{MMT}/\text{G})_4$. Insets are magnified images.

In recent years, the conductive porous sponges with high conductivity and excellent elasticity have been fabricated by the integration of highly elastic polymeric sponge and conductive nanoparticles.^{18,35–45} The inherent agglomeration of conductive nanoparticles among conductive porous sponges normally affects the stability and reliability of the conductive network, and thus, inevitably reduces the mechanical elasticity and durability of as-fabricated piezoresistive sensors. Besides, heat-labile and flammable polymer sponges are usually used as the structural substrates, which hinder their applications in high-temperature and combustion environments. Therefore, the development of emerging spongy conductors with high elasticity, excellent flame retardancy, and high piezoresistive sensitivity is highly demanded yet challenging.

Herein, a sponge-constrained network assembly strategy is presented for fabricating a lightweight, superelastic, and fatigue-resistant spongy conductor. Highly conductive graphene (Gr) and flame-retardant montmorillonite (MMT) were alternately assembled onto a three-dimensional (3D) melamine scaffold. Compared with the traditional compounding methods, the sponge-constrained network assembly strategy is capable of accurately controlling the ratios and contents of desirable components among the resultant composites. The spongy conductor inherited the combined superelastic, highly conductive, and flame-retardant performances from the ternary ingredients. The as-obtained spongy conductor exhibited a highly deformation-tolerant conductivity up to an 80% strain and excellent fatigue resistance of 10,000 cycles at a 70% strain, owing to the achievement of efficient stress dissipations from the 3D spongy scaffold to the high-modulus MMT/G coatings. The resultant spongy conductor inherited the combined superelastic, highly conductive, and flame-retardant performances from the ternary ingredients. As a proof-of-concept, a wearable

piezoresistive sensor using the spongy conductor has been demonstrated, exhibiting high sensitivity, excellent cycling stability, high thermal stability, and flame retardancy. The stable piezoresistive signal output can be maintained at 250 °C for 7 days and under combustion for 20 s. Therefore, the sponge-constrained network assembly strategy provides new ideas for the construction of lightweight, superelastic, and function-tailored spongy conductors for wearable piezoresistive sensors with high sensitivity, wide detecting range, and excellent fatigue resistance in extremely high-temperature and flaming environments.

2. EXPERIMENTAL SECTION

2.1. Materials. MS was obtained from FoamTech Nano Materials Co., Ltd., P. R. China. Natural graphite powder (325 meshes) was obtained from Alfa Aesar. Polyetherimide (PEI) solution ($M_w = 70,000$, 50 wt % in water) was obtained from Aladdin Chemicals. MMT (Cloisite Na⁺) was obtained from Southern Clay Products. Deionized water was used throughout the experiments. All other reagents were provided by Sinopharm Chemicals and without further purifications. Graphene oxide (GO) was prepared according to a Hummers' method.

2.2. Fabrication of the $\text{MS}-(\text{MMT}/\text{G})_n$, $\text{MS}-\text{MMT}_3$, and $\text{MS}-\text{G}_3$. The $\text{MS}-(\text{MMT}/\text{GO})_n$ refers to the melamine sponge (MS) coated with alternating MMT/GO layers, where “ n ” is the number of deposition cycles during the sponge-constrained network assembly. Aqueous dispersion of MMT (1 mg mL^{-1}) was prepared by vigorously stirring 1.0 g of MMT in 1 L of water for 24 h. The as-obtained dispersion was settled to remove impurities for subsequent use. Aqueous dispersion of GO (1 mg mL^{-1}) was prepared by sonicating 1.0 g of GO in 1 L of water for 30 min. For 1 cycle in the sponge-constrained network assembly strategy, the MS was immersed in a cationic solution (PEI, 1 mg mL^{-1}), anionic dispersion (MMT), cationic solution (PEI, 1 mg mL^{-1}), and anionic dispersion (GO) for 1 min in sequence, and each adsorption step was followed by water washing and nitrogen gas drying. Cycled assemblies were repeated to

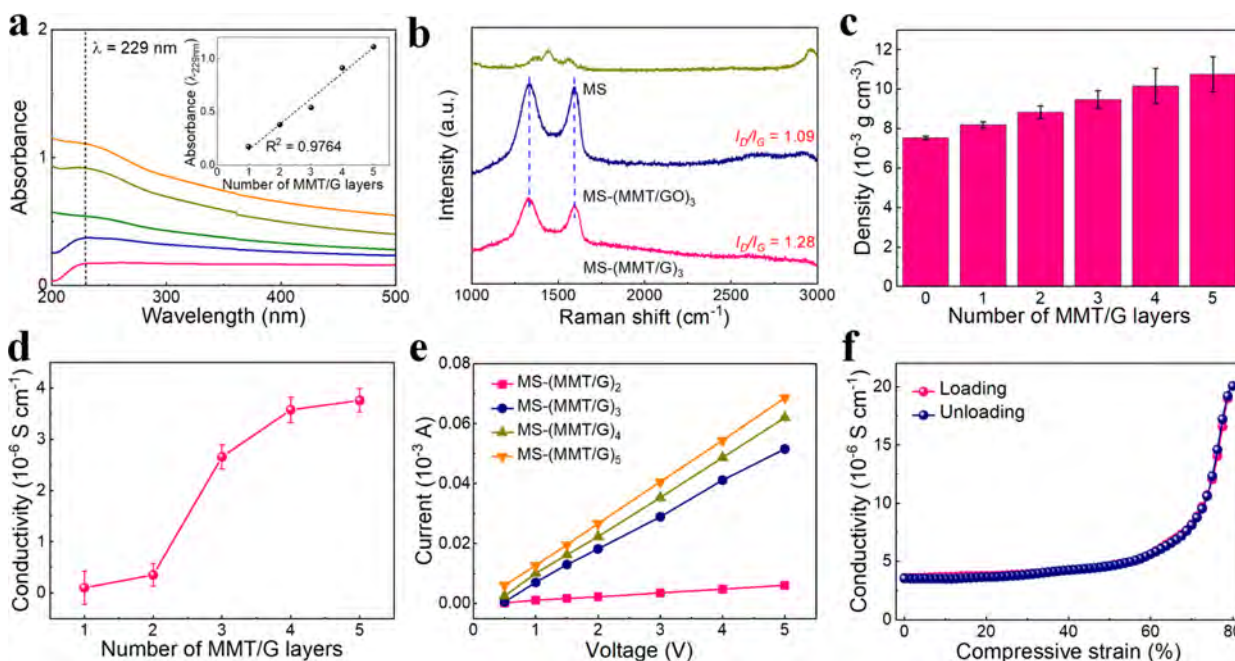


Figure 2. (a) UV-vis spectra for quartz-supported MMT/G ultrathin films. Inset of (a) showing absorbance at 229 nm plotted against the deposition number. (b) Raman spectra of MS, MS-(MMT/GO)₃, and MS-(MMT/G)₃. (c) Densities of MS and MS-(MMT/G)_n. (d) Electrical conductivities of MS-(MMT/G)_n. (e) Current-voltage curves of MS-(MMT/G)_n. (f) Electrical conductivities of MS-(MMT/G)₃ under compressive loading and unloading at 80% strain (voltage: 3 V, compression rate: 50 mm min⁻¹).

achieve the desired number of MMT/GO layers on the MS. The MS-(MMT/G)_n was then prepared by immersing the MS-(MMT/GO)_n in a 50% hydrazine hydrate solution at 90 °C for 1 h, followed by washing with water, and dried in vacuum at 50 °C for 12 h. For comparison, the MS-MMT₃ and MS-GO₃ refer to the MS coated with 3 cycles of MMT and GO layers, respectively. The MS-G₃ was then prepared using a similar reduction method of converting MS-(MMT/GO)₃ into MS-(MMT/G)₃.

2.3. Measurements of the Piezoresistive Sensor. The top and bottom sides of the as-fabricated spongy conductor (30 × 30 × 30 mm³) were connected to copper foil with silver pastes. The piezoresistive sensing performance of the spongy conductor was measured on a digital source meter (Keithley 2400) and loadings of compressive strains were performed by a universal testing machine (UTM2000, SUNS). All graphics are entirely author created and owned. Typically, the graphic in Figure 1a is designed and created by the first author (Mr. Zhichong Liu). All wearable piezoresistive sensing experiments were conducted with the volunteer (the third author), and corresponding graphics were taken by the first author with a digital camera.

2.4. Computational Models and Methods. Finite element modeling (FEM) was performed by using Abaqus. The FEM was conducted in the linear elastic region of the materials to simplify the calculation. The respective material properties of MS and MS-(MMT/G)_n, such as Young's modulus and Poisson's ratio, are listed in Table S1. The sizes of MS and MS-(MMT/G)_n were assigned at a length and width of 10 and 3.4 μm, respectively. The model of MS was composed of a C3D4 element type using 127,446 elements and 192,952 nodes. The inner substrate and outer coating of MS-(MMT/G)_n were partitioned. The inner substrate was composed of C3D4 element types like that of MS. The thickness of the MMT/G layer among the MS-(MMT/G)_n was assigned as 100 nm. The model of MS-(MMT/G)_n was composed of a C3D4 element type using 286,335 elements and 298,391 nodes. The loading was applied from both ends to the middle, and the load force was set as 9 × 10⁻⁵ N.

3. RESULTS AND DISCUSSION

The fabrication procedure for a spongy conductor of the MS-(MMT/G)_n through a sponge-constrained network assembly strategy is illustrated in Figure 1a. The fabricating principle is the achievement of alternating depositions of oppositely charged polyelectrolytes (polyethyleneimine, PEI) and two-dimensional (2D) nanoparticles of Gr and MMT on a 3D porous scaffold of MS. Upon the sponge-constrained network assembly, a highly conductive spongy conductor was achieved by chemically reducing GO into Gr within the MS-(MMT/G)_n. The “n” in the MS-(MMT/G)_n refers to the number of deposition cycles of MMT/G layers on the MS scaffold. Under the constant adsorption time of each layer, the thickness of the assembled multilayers can be precisely controlled by tailoring the number of deposition cycles. Among the MS-(MMT/G)_n, the 3D MS substrate provides an excellent compression resilience depending on its 3D porous scaffold structure. Meanwhile, the MMT/G layers endow the resultant MS-(MMT/G)_n with excellent electrical conductivity and thermal stability.

The microstructures of MS-(MMT/G)_n were accurately controlled by tailoring the deposition numbers. Looking at the morphology of the pristine MS, a 3D open-cell scaffold structure within the MS (Figure 1b,c) accelerated the penetration of the aqueous dispersion through macropores during the assembly.⁴⁶ With an increased assembly number of MMT/G layers, wrinkled structures on the surface gradually came up, while the open-pore structure was maintained (Figure 1d,f,h). It is worth mentioning, the microstructure of the spongy substrate and assembled layers were well maintained after the chemical reduction (Figures S1 and S2). Meanwhile, no aggregation can be observed on the surface of the scaffolds, even in the MS-(MMT/G)₄. This indicates that the MMT and Gr ultrathin layers are well assembled on the spongy substrate according to an electrostatic force-driving assembly. According to Figure 1e,g,i, the thicknesses of MMT/G layers grew linearly with an

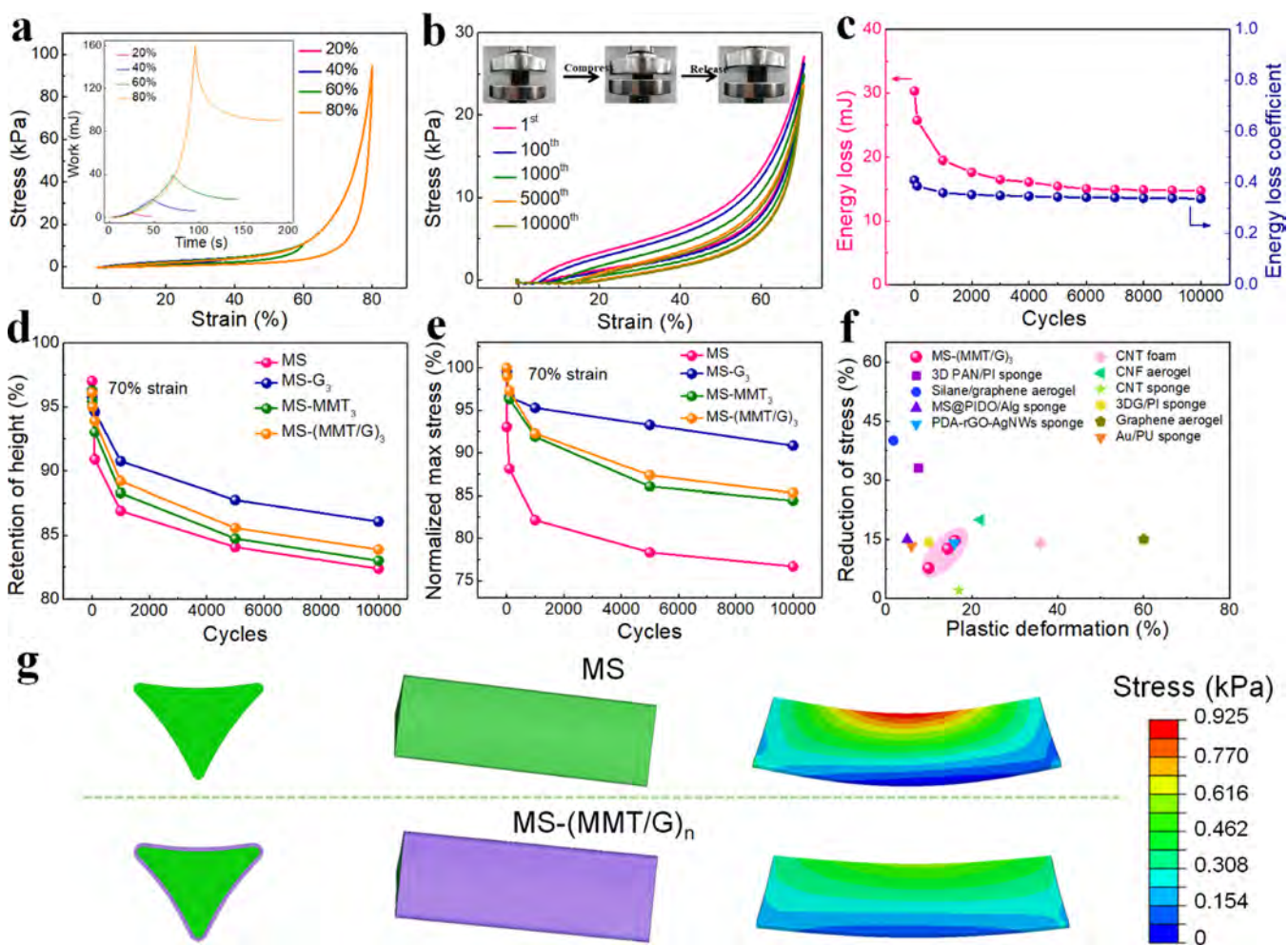


Figure 3. (a) Stress–strain curves of MS-(MMT/G)₃ at various compressive strains. Inset of (a) showing compression work at various strains. (b) Stress–strain curves of MS-(MMT/G)₃ under cyclic compressive loading. Inset of (b) showing its reversible compression behaviors. (c) Cycle-dependent energy loss and energy loss coefficient for MS-(MMT/G)₃. Cycle-dependent (d) retention of height and (e) normalized maximum stress of MS, MS-G₃, MS-MMT₃, and MS-(MMT/G)₃ at 70% strain. (f) Comparison of plastic deformation and reduction of stress of MS-(MMT/G)₃ with other conductive sponges in the literature. (g) FEM analysis for MS and MS-(MMT/G)_n under compression.

increased number of assembly layers, which were ~ 48 , 73, and 98 nm for MS-(MMT/G)₂, MS-(MMT/G)₃, and MS-(MMT/G)₄, respectively.

Ultrathin films of GO, MMT, and MMT/GO were deposited on quartz substrates to investigate the structural evolution of assembled layers on the MS through electrostatic interactions. Figure S3 shows the UV–vis spectra of GO and MMT ultrathin films with increased assembly numbers, respectively. The GO ultrathin film exhibited a strong absorption peak at ~ 230 nm (Figure S3a), corresponding to an orbital transition from π to π^* of C=C bonds within the benzene ring of GO.^{47,48} The MMT ultrathin film showed a strong absorption peak at ~ 227 nm (Figure S3b), corresponding to the characteristic band of MMT related to the transition caused by charge transfer of metal cations.⁴⁹ The MMT/GO ultrathin film showed a strong absorption peak at ~ 229 nm (Figure 2a), which was the synergy effect of the stacked GO and MMT layers, that is, ~ 230 nm for the benzene ring of GO and 227 nm for MMT. The inset of Figure 2a shows that the intensities of the strong absorption bands increased linearly (residual sums of squares close to 1) with an increasing number of assembly layers. This proves that the thickness and content of alternating layers on the surface of

the MS can be easily controlled by the sponge-constrained network assembly.

The MS-(MMT/G)_n was achieved by the chemical reduction of the MS-(MMT/GO)_n. Raman spectra show that the π -conjugated network within GO nanosheets is gradually recovered during the reduction process (Figure 2b). The MS-(MMT/GO)_n and MS-(MMT/G)_n showed two typical Raman peaks at 1340 and 1590 cm^{-1} , corresponding to the D-band of disordered carbon and G-bands of sp^2 carbon.^{50–52} The intensity ratio of the D-band to G-band (I_D/I_G) reflects the disorder degree of carbon structures.^{53–55} The I_D/I_G of MS-(MMT/G)₃ was 1.28, significantly higher than that of MS-(MMT/GO)₃ (1.09). The higher I_D/I_G value reflected that the average size of the sp^2 domains decreased by the reduction of GO nanosheets, along with the formation of more numerous graphitic domains.

The assembly of the MMT/G layers on scaffolds maintained the advantages of lightweight and good air permeability of sponge porous scaffolds. The apparent densities of the MS-(MMT/G)₅ increased slightly to $10.75 \times 10^{-3} \text{ g cm}^{-3}$ from 7.53×10^{-3} for pristine MS (Figure 2c). Meanwhile, the electrical conductivity of MS-(MMT/G)_n was strongly dependent on the number of MMT/G layers. The increasing trend with the

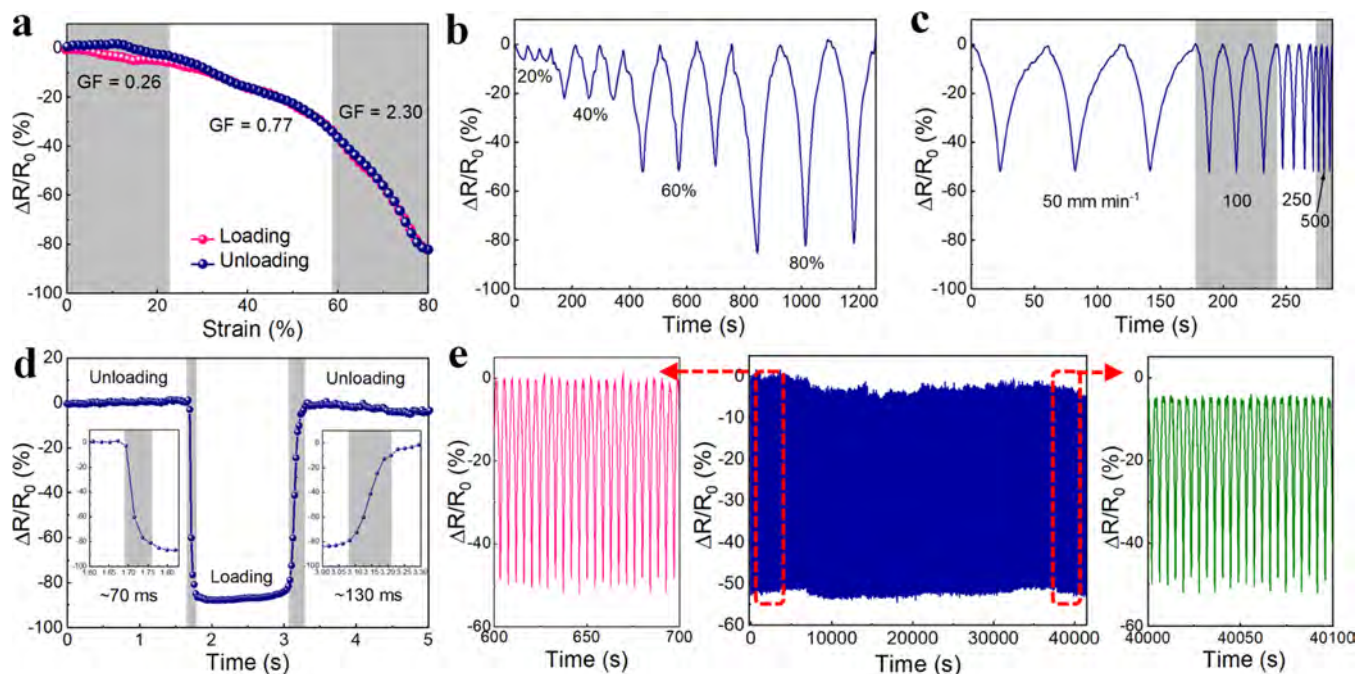


Figure 4. Piezoresistive responses of MS-(MMT/G)₃. (a) Relative resistance change as a function of compressive strains. (b) Relative resistance change at strains of 20, 40, 60, and 80% under a constant compression rate of 10 mm min⁻¹. (c) Relative resistance change with a constant strain of 60% under compressive speeds of 50, 100, 250, and 500 mm min⁻¹. (d) Relative resistance change showing the response time during loading and unloading. (e) Durability test for 10,000 cycles at a 60% strain.

number of assembly layers (Figure 2d) exhibited a big jump from 0.35×10^{-6} to 2.66×10^{-6} S cm⁻¹ with MMT/G layers increased from 2 to 3. This is attributed to a continuous percolating conductive network being formed within the MS-(MMT/G)₃. The conductive network of MS-(MMT/G)₃ reached a stable percolation structure when the electrical conductivity tended to be stable from MS-(MMT/G)₄. The linear characteristics of the *I*-*V* curves (Figure 2e) showed the resistances of MS-(MMT/G)_{*n*} were stable in a wide voltage range of 0–5 V. Under compressive loading and unloading at 80% strain, the MS-(MMT/G)₃ exhibited a stable piezoresistive response under various compressive strains (Figure 2f). The electrical conductivity of the MS-(MMT/G)₃ increased with the increase of compressive strain and completely recovered with unloading. This stable real-time response under various voltages and strains indicated the great potentials of MS-(MMT/G)₃ in applications of piezoresistive sensors.

Mechanical properties and fatigue resistance are important parameters for the development of high-performance piezoresistive materials. Especially, when piezoresistive materials are applied as wearable electronics, the ability to withstand large and complex deformations is necessary.^{56–59} The as-fabricated MS-(MMT/G)₃ revealed excellent mechanical resilience at a strain of 80% and a compressive rate of 200 mm min⁻¹ (Movie S1). Figure 3a exhibits typical stress–strain curves of the MS-(MMT/G)₃ with various compressive strains under cyclic loading and unloading. Three typical regions among the stress–strain curves were observed in the MS-(MMT/G)₃. When the compressive strain was less than 10%, the stress increased rapidly in a linear elastic region. The further increase of compressive strain into 60% caused a plateau region with the slowly increased stress of the MS-(MMT/G)₃. When the compressive strain further increased to 80%, a compact region with sharply rising stress was observed. After being unloaded, no residual strain of the released MS-(MMT/G)₃ indicated its high mechanical

resilience. The introduction of rigid MMT/G multilayers on the surface of the MS skeleton enhanced the compression modulus of MS-(MMT/G)₃ compared to MS but kept the similar shapes of stress–strain curves (Figure S4a).^{60,61} The compression work of the MS-(MMT/G)₃, as shown in inset of Figure 3a, shows that an energy loss is more significant at 80% strain. To understand the fatigue resistance of MS-(MMT/G)₃, stress–strain curves of the MS-(MMT/G)₃ and MS have been recorded during 10,000 compressive cycles at 70% strain (Figures 3b and S4b). The reduction of stress (14.7%) and plastic deformation (16.1%) for the MS-(MMT/G)₃ were significantly lower than those of MS (reduction of stress rate: 23.4%, plastic deformation rate: 17.7%). This excellent elastic- and fatigue-resistant performance was attributed to MMT/G multilayers on the MS skeleton being in favor of efficient energy dissipations. The energy loss coefficient (η) of MS-(MMT/G)₃ under various compression cycles was calculated by eq 1

$$\eta = \frac{\Delta U}{U} \quad (1)$$

where *U* is the compression work and ΔU refers to energy loss. Taking the first compression cycle of MS-(MMT/G)₃ as an example, the *U* was 74.1 mJ. When the pressure was unloaded, the ΔU was measured as 30.3 mJ. In the first cycle, the energy loss of MS-(MMT/G)₃ was 0.41, which mainly came from its plastic deformation, extensive damage of the MS structure, and friction between adjacent skeletons. After 5000 compressive cycles, the energy loss and energy loss coefficient of MS-(MMT/G)₃ remained at 14.7–15.4 mJ and 0.34, respectively (Figure 3c). The near-constant energy loss and energy loss coefficient verified the excellent elastic- and fatigue-resistant properties of MS-(MMT/G)₃. The retention of height and normalized maximum stress of the MS-G₃, MS-MMT₃, MS-(MMT/G)₃, and MS were measured at 70% strain for 10,000 compressive cycles (Figure 3d,e). Compared to MS, with a flat downward

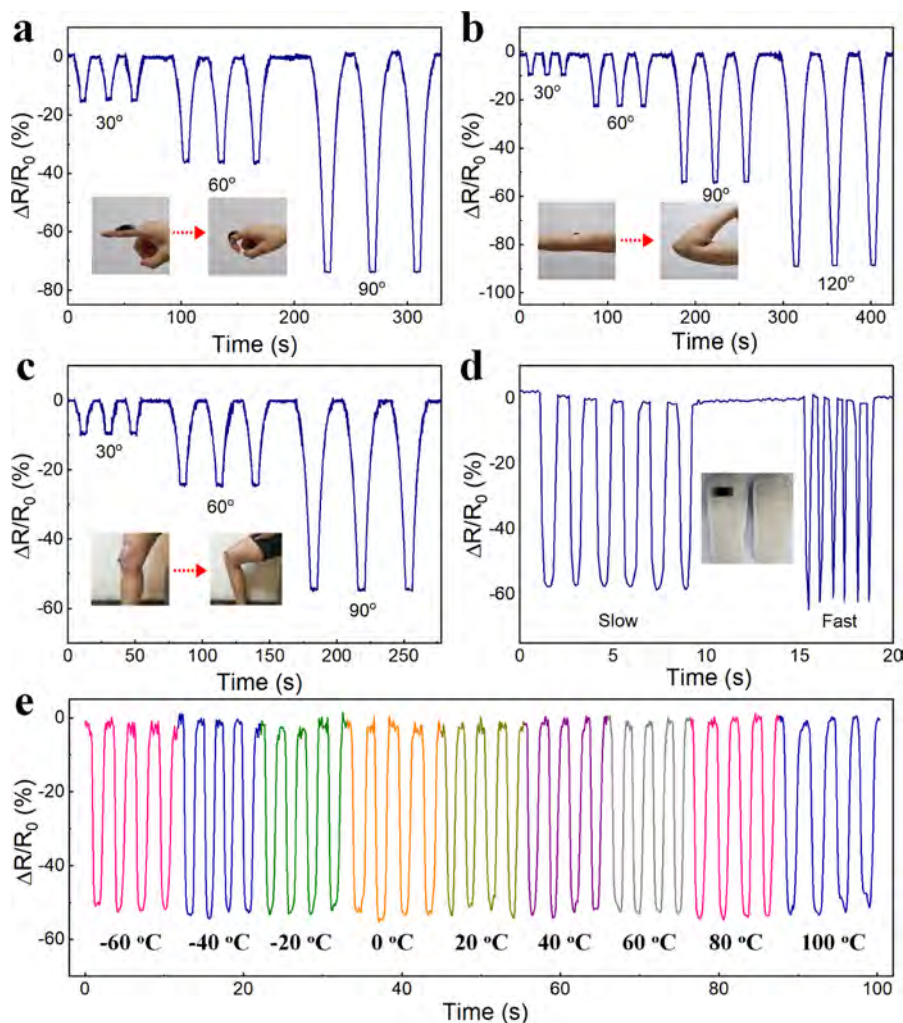


Figure 5. Human motion detection using the MS-(MMT/G)₃ piezoresistive sensor. Relative resistance changes in monitoring (a) finger bending, (b) wrist bending, (c) knee bending, and (d) stamping. (e) Relative resistance changes under 60% strain at temperatures ranging from -60 to 100 °C.

trend on both retention of height and normalized maximum stress with the number of cycles, the MS-(MMT/G)₃ showed better fatigue-resistant properties. This is attributed to its efficient stress dissipations upon deformation. The downward trend of the cyclic curve of MS-MMT₃ was greater than that of MS-G because of the elastic mismatching between the MMT multilayer and spongy skeleton. In constant, the introduction of additional Gr layers among the MS-(MMT/G)₃ improved this. Young's moduli of MS and MS-(MMT/G)₃ were measured during the cyclic compression tests (Figure S5). After 10,000 cycles, the modulus retention of MS (23.8%) was much lower than that of MS-(MMT/G)₃ (56.4%). The presence of MMT/G layers was beneficial to the stress dissipation with largely improved stability of spongy structures. Compared to conductive aerogel and sponge samples in the literature, the MS-(MMT/G)₃ showed a smaller plastic deformation as well as a lower rate of stress reduction (Figure 3f).^{62–71} The FEM analysis for the MS and MS-(MMT/G)_n under deformation has been used to further understand the high fatigue resistance of MS-(MMT/G)_n. The deformation of the model spline was used to simulate foam materials during deformation. Different from the stress distribution on the surface of the MS spline which was relatively concentrated, the overall deformation of the MS-(MMT/G)_n spline was much smaller and the stress distribution was largely dissipated. The MMT/G multilayer could dissipate

efficient stress during deformation for achieving high fatigue resistance of MS-(MMT/G)_n.

Figure 4 shows the piezoresistive sensing performance of the MS-(MMT/G)₃. Figure 4a shows the relative resistance changes ($\Delta R/R_0$, the R_0 and ΔR represent the initial resistance and resistance change) of the MS-(MMT/G)₃ with various compressive strains (ϵ) from 0 to 80%. The gauge factor (GF) is the slope of the linear region of the curve, calculated as follows

$$GF = \frac{\Delta R/R_0}{\epsilon} \quad (2)$$

The $\Delta R/R_0$ of the MS-(MMT/G)₃ sensor decreased monotonically with an increasing compressive strain. The conductive network of MS-(MMT/G)₃ was gradually densified with the increase of the contact area of the skeleton, leading to an improvement of the conductivity. The sensitivity of MS-(MMT/G)₃ increased in three stages during the strain range of 0–80%. In the strain region of 60–80%, the MS-(MMT/G)₃ showed the highest GF value of 2.3. This was explained by the most evident bending deformation of the 3D skeleton structure within the MS-(MMT/G)₃ under a large strain. The linearity of the three stages was calculated to be 0.72, 0.98, and 0.99, respectively. The resistance changes of MS-(MMT/G)₃ under a low strain were mainly determined by the tunnel effect between

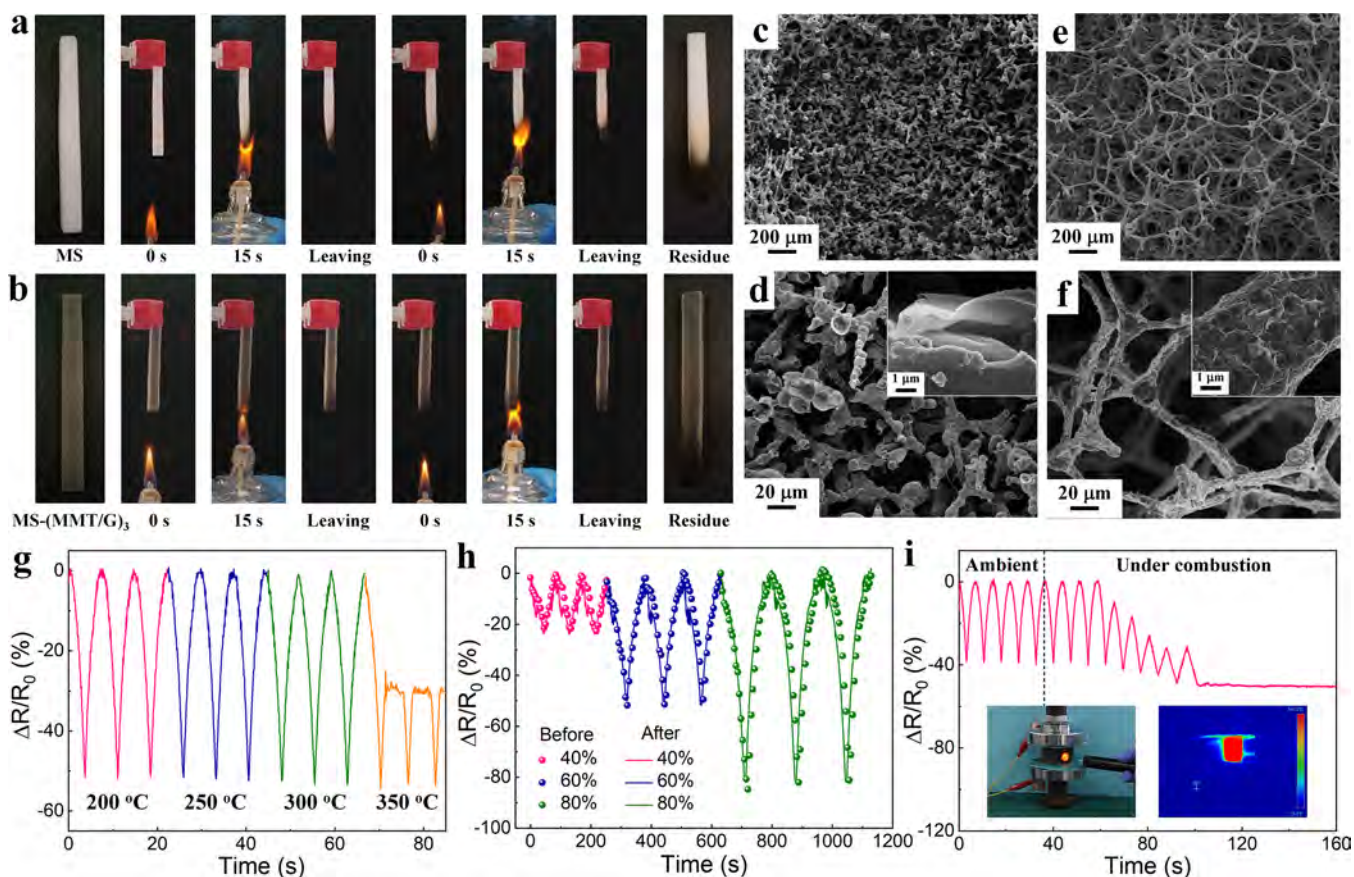


Figure 6. Thermal stability and flame retardancy of MS-(MMT/G)₃ and piezoresistive sensor. Vertical flammability tests for (a) MS and (b) MS-(MMT/G)₃ with an alcohol burner for 30 s. SEM images of (c,d) MS and (e,f) MS-(MMT/G)₃ after flammability tests. Insets are magnified images. (g) Relative resistance change of the sensor before and after heat treatment at various high temperatures for 1 day. (h) Relative resistance change under various compressive strains before and after heat treatment at 250 °C for 7 days. (i) Durability test of the sensor under combustion. Insets of (i) showing optical and infrared images of the sensor burned by a cigarette lighter after 10 s.

the adjacent conductive nanoparticles. The nonlinear growth index of resistance was caused by the tunnel effect and imperfect conductive path. The resistance changes caused by the contact of conductive layers were the main mechanism at a relatively large strain, and more contribution of the contact of conductive paths for resistance changes was capable of realizing better linearity. Compared to other conductive sponges in the literature,^{63,65,72–79} the MS-(MMT/G)₃ showed higher sensitivity in a relatively large strain range (Figure S6). Several conductive sponges impregnated with an elastomer matrix might exhibit a high gauge factor but their applications were largely limited at a small compressive strain. The resistance responses of the MS-(MMT/G)₃ sensor at the strains of 20, 40, 60, and 80% are shown in Figure 4b. With an increased strain, the MS-(MMT/G)₃ sensor showed a fast and synchronous increasing resistance change. The stable resistance responses under different strains indicate the wide working range of the MS-(MMT/G)₃ sensor. The MS-(MMT/G)₃ sensor also exhibited the potential for the application of high-frequency and real-time human motion detection.⁸⁰ The resistance responses, as shown in Figure 4c, exhibit stable signal peaks at various compressive rates as well as constant signals at the same compression rate. MS-(MMT/G)₃ also showed a fast response property which ensured the synchronic monitoring for various external stimuli. The response time and recovery time of the MS-(MMT/G)₃ sensor at 80% strain were 70 and 130 ms, respectively (Figure 4d). Durability and stability of the MS-

(MMT/G)₃ sensor at a strain of 60% for 10,000 continuous cycles are shown in Figure 4e. After 10,000 cycles of applied pressure, only 4.1% resistance response of the MS-(MMT/G)₃ sensor has been changed. The slight decrease of response signal peaks was caused by the inevitable plastic deformation of the 3D skeleton structure during compression. The MMT/G layer was tightly attached to the skeleton after the durability test. The MS-(MMT/G)₃ kept the whole intact morphology, showing its excellent structural stability (Figure S7). MS-G₃ was also assembled for piezoresistive sensing performance. It is worth mentioning that the introduction of the MMT layer has no obvious negative impacts on the MS-(MMT/G)₃, as the MS-G₃ sensor showed similar response signals as the MS-(MMT/G)₃ sensor (Figure S8).

Figure 5 demonstrates the applications of the MS-(MMT/G)₃ sensor for human motion detection. For finger bending detection, the MS-(MMT/G)₃ sensor was attached to the finger joints using a medical tape (Figure 5a). The relative resistance of the MS-(MMT/G)₃ sensor decreased with the bending of the finger and increased with the extension of the finger. The peak value of the resistance response corresponded to the bending angle of the finger (30, 60, and 90°), indicating that the MS-(MMT/G)₃ sensor possessed the potential in detecting common joint bending motions. The MS-(MMT/G)₃ sensor was also attached to the wrist and knee for large body motion detection (Figure 5b,c). The MS-(MMT/G)₃ sensor showed stable and repeatable relative resistance responses according to

the bending and recovery of the wrist and knee. The MS-(MMT/G)₃ sensor was also attached to the sole of the shoe for stamping motion detection (Figure 5d). The MS-(MMT/G)₃ sensor showed stable and repeatable relative resistance responses at different stamping speeds. The relative resistances of the MS-(MMT/G)₃ sensor increased when the shoe fell on the ground and decreased when the shoe lifted. The MS-(MMT/G)₃ sensor exhibited periodically relative resistance responses under slow and fast walking conditions. The peak value of the resistance response was stable and repeatable, showing a stable resistance response property of the MS-(MMT/G)₃ sensor. Considering that there is little change in the walking distance for an adult, the walking speed and distance could be calculated by the average value and the total number of the peak value. These examples indicate that the MS-(MMT/G)₃ sensor possesses great potential in human health and sports monitoring.

Wearable sensors are subject to the constant changes of external temperatures in daily use, and therefore, it is particularly important for wearable sensors to stably detect human motions at various external temperatures. The electrical conductivity of the MS-(MMT/G)₃ exhibited a nearly linear increasing relationship with the external temperature in the range of -60 to 100 °C (Figure S9a), which was consistent with that of graphene materials in the literature.⁸¹ Besides, the conductivities were stably maintained at different temperatures (-40, 0, 40, and 80 °C) over 1000 s (Figure S9b). The high applicability in a wide temperature range has been further proved by performing the MS-(MMT/G)₃ sensor at various temperatures (Figure 5e). The stable and repeatable relative resistance changing at a strain of 60% under different temperatures from -60 to 100 °C indicated the excellent compressive resilience and resistance stability of the MS-(MMT/G)₃ sensor over a wide temperature range.

Figure 6 shows the thermal stability and flame-retardant performance of the MS-(MMT/G)₃ sensor. MS and MS-(MMT/G)₃ has different flame retardancy under the 30 s vertical combustion. The flame propagation speed of the MS-(MMT/G)₃ was much slower than that of MS (Figure 6a). The MS kept burning for 15 s and was quickly ignited again when it was exposed to flame for another 15 s. MS further collapsed after combustion while the MS-(MMT/G)₃ maintained the integrity of the macrostructure after combustion (Figure 6b). The microstructures of the MS and MS-(MMT/G)₃ after vertical combustion tests were characterized. Scanning electron microscopy (SEM) images of the MS after combustion (Figure 6c,d) showed that more voids were formed between the adjacent skeleton structures. The reason for the 3D structure of the MS collapses is the degradation and carbonization at high temperatures. The MS-(MMT/G)₃ maintained the good integrity of microstructure and tightly attached MMT/G layers after combustion (Figure 6e,f). Wrinkled structures formed on the surface of the spongy skeleton among MS-(MMT/G)₃ is the result of MMT/G layers shrinkage during combustion. Ethanol combustion tests were also performed on the MS and MS-(MMT/G)₃ (Figure S10a,b). The MS-(MMT/G)₃ maintained the integrity of the macrostructure with a higher mass residual (35.4%) than that of MS (25.1%). Both vertical combustion and ethanol combustion tests show that the flame retardancy of MS-(MMT/G)₃ is largely improved by the introduction of the MMT/G layer.

Figure 6g shows the relative resistance response of the MS-(MMT/G)₃ sensor before and after heat treatment. The stable

and repeatable resistance responses of MS-(MMT/G)₃ sensor can be kept under 1-day treatments at 300 °C. After being heat treated for 7 days, the stability can be maintained under 250 °C (Figure S11). For 1-day treatment, the initial relative resistance value of the MS-(MMT/G)₃ sensor showed a significant decrease at 350 °C. This was because a certain degree of plastic deformation had taken place among MS-(MMT/G)₃ during the high-temperature treatment. Figure 6h shows the relative resistance response of the MS-(MMT/G)₃ sensor under various strains after heat treatment at 250 °C for 7 days, and the relative resistance changes before and after high-temperature treatment are represented by scattered points and straight lines. The high coincidence of the scattered points and straight lines indicated that the MS-(MMT/G)₃ sensor had excellent mechanical properties and thermal stability, with long-term high-temperature stability under 250 °C. Furthermore, the sensing properties of the MS-(MMT/G)₃ sensor under combustion were also measured. The MS-(MMT/G)₃ sensor maintained excellent mechanical properties and stable piezoresistive sensing signals under combustion over 20 s (Figure 6i, Movie S2). The initial value of the relative resistance of the MS-(MMT/G)₃ sensor decreased after the fourth cycle, which was because of the damage of the superelastic skeleton structure among the MS-(MMT/G)₃ under combustion after 20 s. The MS-(MMT/G)₃ sensor lost its resilience after complete combustion at 100 s. Resistance changes of the MS-(MMT/G)₃ sensor without loading stress under combustion were also measured (Figure S12). The resistance change curve showed a slight decrease after 10 s, which is because of the decrease of resistance caused by an increase in environmental temperatures. The curve rose sharply at 47 s, which is because of the burning of the sponge resulting in an open circuit. The high thermal stability of MS-(MMT/G)₃ compared with that of MS was also convinced by thermogravimetric analysis (TGA) results (Figure S13). Neat MS began to decompose from 100 °C, and carbonization and dehydrogenation of the spongy substrates occurred after 400 °C. However, the decomposition rate of the spongy substrates increased significantly, and the MS-(MMT/G)₃ showed a higher 5% weight loss temperature (120 °C) and mass residual (12%) than those of MS (115 °C, 8%) because the MMT layer significantly improved the thermal stability of the MS-(MMT/G)₃. The thermal conductivity of MS-(MMT/G)₃ is 26.5 mW m⁻¹ K⁻¹ at room temperature, which is close to that of air. The MS-(MMT/G)₃ had a similar thermal conductivity to the aerogel insulation materials reported in other literature studies (Table S2),^{82–85} and therefore showed high potential as an intelligent thermal insulation material.

4. CONCLUSIONS

In summary, a sponge-constrained network assembly strategy is presented for assembling the MMT and Gr nanosheets on the 3D porous scaffolds of MS. The sponge-constrained network assembly strategy is capable of accurately controlling the microstructure and physical properties of MS-(MMT/G)_n by tailoring the assembly numbers of MMT/G layers on the sponge. The resultant MS-(MMT/G)_n exhibited unique features of lightweight, good elasticity, high conductivity, and excellent fatigue resistance, owing to the achievement of efficient stress dissipation from the 3D spongy scaffold to the high-modulus MMT/G coatings. The as-obtained MS-(MMT/G)₃ showed low reduction of stress and plastic deformation of 14.7 and 16.1%, respectively, after 10,000 compressive cycles at a strain of 70%. The piezoresistive MS-(MMT/G)₃ sensor

demonstrated a stable piezoresistive sensing response over a wide strain range up to 80%. The MS-(MMT/G)₃ can readily work as a wearable sensor by monitoring large-strain human motions in real-time, such as finger/wrist/knee bending and stamping movements. More importantly, the MS-(MMT/G)₃ sensor exhibited excellent thermal stability and flame retardancy, showing stable and real-time human motion detection in a wide temperature range from -60 to 250 °C and even under a combustion condition for at least 20 s. This work, therefore, provides new ideas for the construction of spongy conductors with high piezoresistive sensitivity and durability for human motion detection under extremely harsh high-temperature and flaming conditions.

■ ASSOCIATED CONTENT

Supporting Information

The Supporting Information is available free of charge at <https://pubs.acs.org/doi/10.1021/acsami.0c20852>.

Materials, characterizations; SEM images of MS-GO₃, MS-MMT₃ and MS-(MMT/GO)₃, hydrazine hydrate-treated MS, MS-GO₃ and MS-MMT₃; UV-vis spectra for Gr and MMT ultrathin films; stress-strain curves of MS; Young's modulus of MS and MS-(MMT/G)₃ in cyclic tests; sensing performance of MS-(MMT/G)₃ sensor compared with conductive sponges in the literature; SEM images of MS-(MMT/G)₃ after 10,000 compressive cycles at a strain of 60%; piezoresistive response of MS-G₃ sensor; temperature-dependent electrical properties of MS-(MMT/G)₃; photographs of ethanol-soaked MS and MS-(MMT/G)₃ during burning and after combustion; piezoresistive response of the MS-(MMT/G)₃ sensor after heat treatment; resistance changes of the MS-(MMT/G)₃ sensor under combustion; TGA curves of MS and MS-(MMT/G)₃; and tables summarizing the parameters for FEM analysis and the thermal conductivities of MS-(MMT/G)₃ compared with aerogel insulation materials in the literature (PDF)

Cyclic compressive performance of MS-(MMT/G)₃ (AVI)

Piezoresistive responses of MS-(MMT/G)₃ sensor exposed to flame (AVI)

■ AUTHOR INFORMATION

Corresponding Author

Chao Zhang – State Key Laboratory for Modification of Chemical Fibers and Polymer Materials, College of Materials Science and Engineering, Innovation Center for Textile Science and Technology, Donghua University, Shanghai 201620, P. R. China; orcid.org/0000-0003-1255-7183; Email: czhang@dhu.edu.cn

Authors

Zhichong Liu – State Key Laboratory for Modification of Chemical Fibers and Polymer Materials, College of Materials Science and Engineering, Innovation Center for Textile Science and Technology, Donghua University, Shanghai 201620, P. R. China

Kening Wan – School of Engineering and Materials Science, Queen Mary University of London, London E1 4NS, U.K.

Tianyi Zhu – State Key Laboratory for Modification of Chemical Fibers and Polymer Materials, College of Materials Science and Engineering, Innovation Center for Textile Science

and Technology, Donghua University, Shanghai 201620, P. R. China

Jixin Zhu – Shaanxi Institute of Flexible Electronics (SIFE), Northwestern Polytechnical University (NPU), Xi'an 710072, P. R. China; orcid.org/0000-0001-8749-8937

Jingsan Xu – School of Chemistry, Physics and Mechanical Engineering, Queensland University of Technology, Brisbane, Queensland 4001, Australia; orcid.org/0000-0003-1172-3864

Tianxi Liu – State Key Laboratory for Modification of Chemical Fibers and Polymer Materials, College of Materials Science and Engineering, Innovation Center for Textile Science and Technology, Donghua University, Shanghai 201620, P. R. China; Key Laboratory of Synthetic and Biological Colloids, Ministry of Education, School of Chemical and Material Engineering, Jiangnan University, Wuxi 214122, P. R. China; orcid.org/0000-0002-5592-7386

Complete contact information is available at:

<https://pubs.acs.org/doi/10.1021/acsami.0c20852>

Author Contributions

The manuscript was written through contributions of all the authors. All the authors have given approval to the final version of the manuscript.

Notes

The authors declare no competing financial interest.

■ ACKNOWLEDGMENTS

We are grateful for the financial support from the National Natural Science Foundation of China (51773035), Ministry of Education of the People's Republic of China (6141A02033233), the Shanghai Scientific and Technological Innovation Project (18JC1410600), and Dr. Yiyu Feng from Tianjin University for the help with finite element method simulations.

■ REFERENCES

- (1) Huang, H.; Han, L.; Wang, Y.; Yang, Z.; Zhu, F.; Xu, M. Tunable Thermal-Response Shape Memory Bio-Polymer Hydrogels as Body Motion Sensors. *Eng. Sci.* **2020**, *9*, 60–67.
- (2) Cai, J.; Xu, W.; Liu, Y.; Zhu, Z.; Liu, G.; Ding, W.; Wang, G.; Wang, H.; Luo, Y. Robust Construction of Flexible Bacterial Cellulose@Ni(OH)₂ Paper: Toward High Capacitance and Sensitive H₂O₂ Detection. *Eng. Sci.* **2019**, *5*, 21–29.
- (3) Su, Y.-F.; Han, G.; Kong, Z.; Nantung, T.; Lu, N. Embeddable Piezoelectric Sensors for Strength Gain Monitoring of Cementitious Materials: The Influence of Coating Materials. *Eng. Sci.* **2020**, *11*, 66–75.
- (4) Chen, J.; Zhu, Y.; Guo, Z.; Nasibulin, A. G. Recent Progress on Thermo-Electrical Properties of Conductive Polymer Composites and Their Application in Temperature Sensors. *Eng. Sci.* **2020**, *12*, 13–22.
- (5) Liu, M.; Pu, X.; Jiang, C.; Liu, T.; Huang, X.; Chen, L.; Du, C.; Sun, J.; Hu, W.; Wang, Z. L. Large-Area All-Textile Pressure Sensors for Monitoring Human Motion and Physiological Signals. *Adv. Mater.* **2017**, *29*, 1703700.
- (6) Takei, K.; Takahashi, T.; Ho, J. C.; Ko, H.; Gillies, A. G.; Leu, P. W.; Fearing, R. S.; Javey, A. Nanowire Active-Matrix Circuitry for Low-Voltage Macroscale Artificial Skin. *Nat. Mater.* **2010**, *9*, 821–826.
- (7) Wang, S.; Xu, J.; Wang, W.; Wang, G.-J. N.; Rastak, R.; Molina-Lopez, F.; Chung, J. W.; Niu, S.; Feig, V. R.; Lopez, J.; Lei, T.; Kwon, S.-K.; Kim, Y.; Foudeh, A. M.; Ehrlich, A.; Gasperini, A.; Yun, Y.; Murmann, B.; Tok, J. B.-H.; Bao, Z. Skin Electronics from Scalable Fabrication of an Intrinsically Stretchable Transistor Array. *Nature* **2018**, *555*, 83–88.
- (8) Kang, D.; Pikhitsa, P. V.; Choi, Y. W.; Lee, C.; Shin, S. S.; Piao, L.; Park, B.; Suh, K.-Y.; Kim, T.-i.; Choi, M. Ultrasensitive Mechanical

Crack-Based Sensor Inspired by the Spider Sensory System. *Nature* **2014**, *516*, 222–226.

(9) Guo, Y.; Zhong, M.; Fang, Z.; Wan, P.; Yu, G. A Wearable Transient Pressure Sensor Made with Mxene Nanosheets for Sensitive Broad-Range Human-Machine Interfacing. *Nano Lett.* **2019**, *19*, 1143–1150.

(10) Chen, S.; Liu, H.; Liu, S.; Wang, P.; Zeng, S.; Sun, L.; Liu, L. Transparent and Waterproof Ionic Liquid-Based Fibers for Highly Durable Multifunctional Sensors and Strain-Insensitive Stretchable Conductors. *ACS Appl. Mater. Interfaces* **2018**, *10*, 4305–4314.

(11) Duan, S.; Wang, Z.; Zhang, L.; Liu, J.; Li, C. Three-Dimensional Highly Stretchable Conductors from Elastic Fiber Mat with Conductive Polymer Coating. *ACS Appl. Mater. Interfaces* **2017**, *9*, 30772–30778.

(12) Lv, Z.; Liu, J.; Yang, X.; Fan, D.; Cao, J.; Luo, Y.; Zhang, X. Naturally Derived Wearable Strain Sensors with Enhanced Mechanical Properties and High Sensitivity. *ACS Appl. Mater. Interfaces* **2020**, *12*, 22163–22169.

(13) Ma, C.; Yuan, Q.; Du, H.; Ma, M.-G.; Si, C.; Wan, P. Multiresponsive Mxene (Ti₃C₂T_x)-Decorated Textiles for Wearable Thermal Management and Human Motion Monitoring. *ACS Appl. Mater. Interfaces* **2020**, *12*, 34226–34234.

(14) Wang, Z.; Zhang, L.; Liu, J.; Li, C. Highly Stretchable, Sensitive, and Transparent Strain Sensors with a Controllable in-Plane Mesh Structure. *ACS Appl. Mater. Interfaces* **2019**, *11*, 5316–5324.

(15) Yan, H.; Zhong, M.; Lv, Z.; Wan, P. Stretchable Electronic Sensors of Nanocomposite Network Films for Ultrasensitive Chemical Vapor Sensing. *Small* **2017**, *13*, 1701697.

(16) Yue, X.; Jia, Y.; Wang, X.; Zhou, K.; Zhai, W.; Zheng, G.; Dai, K.; Mi, L.; Liu, C.; Shen, C. Highly Stretchable and Durable Fiber-Shaped Strain Sensor with Porous Core-Sheath Structure for Human Motion Monitoring. *Compos. Sci. Technol.* **2020**, *189*, 108038.

(17) Zhao, Y.; Ren, M.; Shang, Y.; Li, J.; Wang, S.; Zhai, W.; Zheng, G.; Dai, K.; Liu, C.; Shen, C. Ultra-Sensitive and Durable Strain Sensor with Sandwich Structure and Excellent Anti-Interference Ability for Wearable Electronic Skins. *Compos. Sci. Technol.* **2020**, *200*, 108448.

(18) Ding, Y.; Xu, T.; Onyilagha, O.; Fong, H.; Zhu, Z. Recent Advances in Flexible and Wearable Pressure Sensors Based on Piezoresistive 3d Monolithic Conductive Sponges. *ACS Appl. Mater. Interfaces* **2019**, *11*, 6685–6704.

(19) Wu, X.; Liu, X.; Wang, J.; Huang, J.; Yang, S. Reducing Structural Defects and Oxygen-Containing Functional Groups in GO-Hybridized CNTs Aerogels: Simultaneously Improve the Electrical and Mechanical Properties to Enhance Pressure Sensitivity. *ACS Appl. Mater. Interfaces* **2018**, *10*, 39009–39017.

(20) Jang, S.; Jee, E.; Choi, D.; Kim, W.; Kim, J. S.; Amoli, V.; Sung, T.; Choi, D.; Kim, D. H.; Kwon, J.-Y. Ultrasensitive, Low-Power Oxide Transistor-Based Mechanotransducer with Microstructured, Deformable Ionic Dielectrics. *ACS Appl. Mater. Interfaces* **2018**, *10*, 31472–31479.

(21) Tang, Z.; Jia, S.; Zhou, C.; Li, B. 3D Printing of Highly Sensitive and Large-Measurement-Range Flexible Pressure Sensors with a Positive Piezoresistive Effect. *ACS Appl. Mater. Interfaces* **2020**, *12*, 28669–28680.

(22) Liu, Q.; Yang, S.; Ren, J.; Ling, S. Flame-Retardant and Sustainable Silk Ionotronic Skin for Fire Alarm Systems. *ACS Mater. Lett.* **2020**, *2*, 712–720.

(23) Wu, Q.; Gong, L.-X.; Li, Y.; Cao, C.-F.; Tang, L.-C.; Wu, L.; Zhao, L.; Zhang, G.-D.; Li, S.-N.; Gao, J.; Li, Y.; Mai, Y.-W. Efficient Flame Detection and Early Warning Sensors on Combustible Materials Using Hierarchical Graphene Oxide/Silicone Coatings. *ACS Nano* **2018**, *12*, 416–424.

(24) Li, D.; Bu, X.; Xu, Z.; Luo, Y.; Bai, H. Bioinspired Multifunctional Cellular Plastics with a Negative Poisson's Ratio for High-Energy Dissipation. *Adv. Mater.* **2020**, *32*, 2001222.

(25) Gao, W.; Zhao, N.; Yu, T.; Xi, J.; Mao, A.; Yuan, M.; Bai, H.; Gao, C. High-Efficiency Electromagnetic Interference Shielding Realized in Nacre-Mimetic Graphene/Polymer Composite with Extremely Low Graphene Loading. *Carbon* **2020**, *157*, 570–577.

(26) Chen, C.; Hu, L. Super Elastic and Thermally Insulating Carbon Aerogel: Gotubular Like Polar Bear Hair. *Matter* **2019**, *1*, 36–38.

(27) Pan, F.; Chen, S.-M.; Li, Y.; Tao, Z.; Ye, J.; Ni, K.; Yu, H.; Xiang, B.; Ren, Y.; Qin, F.; Yu, S.-H.; Zhu, Y. 3D Graphene Films Enable Simultaneously High Sensitivity and Large Stretchability for Strain Sensors. *Adv. Funct. Mater.* **2018**, *28*, 1803221.

(28) Wang, J.; Shi, Z.; Wang, X.; Mai, X.; Fan, R.; Liu, H.; Wang, X.; Guo, Z. Enhancing Dielectric Performance of Poly(Vinylidene Fluoride) Nanocomposites Via Controlled Distribution of Carbon Nanotubes and Barium Titanate Nanoparticle. *Eng. Sci.* **2018**, *4*, 79–86.

(29) Zhang, D.; Sun, J.; Lee, L. J.; Castro, J. M. Overview of Ultrasonic Assisted Manufacturing Multifunctional Carbon Nanotube Nanopaper Based Polymer Nanocomposites. *Eng. Sci.* **2020**, *10*, 35–50.

(30) Yan, X.; Liu, J.; Khan, M. A.; Sheriff, S.; Vupputuri, S.; Das, R.; Sun, L.; Young, D. P.; Guo, Z. Efficient Solvent-Free Microwave Irradiation Synthesis of Highly Conductive Polypropylene Nanocomposites with Lowly Loaded Carbon Nanotubes. *ES Mater. Manuf.* **2020**, *9*, 21–33.

(31) Xie, P.; Li, Y.; Hou, Q.; Sui, K.; Liu, C.; Fu, X.; Zhang, J.; Murugadoss, V.; Fan, J.; Wang, Y.; Fan, R.; Guo, Z. Tunneling-Induced Negative Permittivity in Ni/Mno Nanocomposites by a Bio-Gel Derived Strategy. *J. Mater. Chem. C* **2020**, *8*, 3029–3039.

(32) Li, T.; Gao, Y.; Zheng, K.; Ma, Y.; Ding, D.; Zhang, H. Achieving Better Greenhouse Effect Than Glass: Visibly Transparent and Low Emissivity Metal-Polymer Hybrid Metamaterials. *ES Energy Environ.* **2019**, *5*, 102–107.

(33) Zhou, Y.; Wu, S.; Ma, Y.; Zhang, H.; Zeng, X.; Wu, F.; Liu, F.; Ryu, J. E.; Guo, Z. Recent Advances in Organic/Composite Phase Change Materials for Energy Storage. *ES Energy Environ.* **2020**, *9*, 28–40.

(34) Sun, L.; Liang, L.; Shi, Z.; Wang, H.; Xie, P.; Dastan, D.; Sun, K.; Fan, R. Optimizing Strategy for the Dielectric Performance of Topological-Structured Polymer Nanocomposites by Rationally Tailoring the Spatial Distribution of Nanofillers. *Eng. Sci.* **2020**, *12*, 95–105.

(35) Sengupta, D.; Pei, Y.; Kottapalli, A. G. P. Ultralightweight and 3D Squeezable Graphene-Polydimethylsiloxane Composite Foams as Piezoresistive Sensors. *ACS Appl. Mater. Interfaces* **2019**, *11*, 35201–35211.

(36) Cao, M.; Fan, S.; Qiu, H.; Su, D.; Li, L.; Su, J. Cb Nanoparticles Optimized 3D Wearable Graphene Multifunctional Piezoresistive Sensor Framed by Loofah Sponge. *ACS Appl. Mater. Interfaces* **2020**, *12*, 36540–36547.

(37) Guan, X.; Wang, Z.; Zhao, W.; Huang, H.; Wang, S.; Zhang, Q.; Zhong, D.; Lin, W.; Ding, N.; Peng, Z. Flexible Piezoresistive Sensors with Wide-Range Pressure Measurements Based on a Graded Nest-Like Architecture. *ACS Appl. Mater. Interfaces* **2020**, *12*, 26137–26144.

(38) Huang, Y.; Yu, B.; Zhang, L.; Ning, N.; Tian, M. Highly Stretchable Conductor by Self-Assembling and Mechanical Sintering of a 2D Liquid Metal on a 3D Polydopamine-Modified Polyurethane Sponge. *ACS Appl. Mater. Interfaces* **2019**, *11*, 48321–48330.

(39) Wang, L.; Wang, D.; Wu, Z.; Luo, J.; Huang, X.; Gao, Q.; Lai, X.; Tang, L.-C.; Xue, H.; Gao, J. Self-Derived Superhydrophobic and Multifunctional Polymer Sponge Composite with Excellent Joule Heating and Photothermal Performance for Strain/Pressure Sensors. *ACS Appl. Mater. Interfaces* **2020**, *12*, 13316–13326.

(40) Zhang, S.; Liu, H.; Yang, S.; Shi, X.; Zhang, D.; Shan, C.; Mi, L.; Liu, C.; Shen, C.; Guo, Z. Ultrasensitive and Highly Compressible Piezoresistive Sensor Based on Polyurethane Sponge Coated with a Cracked Cellulose Nanofibril/Silver Nanowire Layer. *ACS Appl. Mater. Interfaces* **2019**, *11*, 10922–10932.

(41) Kim, S.; Amjadi, M.; Lee, T.-I.; Jeong, Y.; Kwon, D.; Kim, M. S.; Kim, K.; Kim, T.-S.; Oh, Y. S.; Park, I. Wearable, Ultrawide-Range, and Bending-Insensitive Pressure Sensor Based on Carbon Nanotube Network-Coated Porous Elastomer Sponges for Human Interface and Healthcare Devices. *ACS Appl. Mater. Interfaces* **2019**, *11*, 23639–23648.

(42) Chen, Y.; Zhang, L.; Mei, C.; Li, Y.; Duan, G.; Agarwal, S.; Greiner, A.; Ma, C.; Jiang, S. Wood-Inspired Anisotropic Cellulose

Nanofibril Composite Sponges for Multifunctional Applications. *ACS Appl. Mater. Interfaces* **2020**, *12*, 35513–35522.

(43) Lu, W.; Yu, P.; Jian, M.; Wang, H.; Wang, H.; Liang, X.; Zhang, Y. Molybdenum Disulfide Nanosheets Aligned Vertically on Carbonized Silk Fabric as Smart Textile for Wearable Pressure-Sensing and Energy Devices. *ACS Appl. Mater. Interfaces* **2020**, *12*, 11825–11832.

(44) Chen, Z.; Zhuo, H.; Hu, Y.; Lai, H.; Liu, L.; Zhong, L.; Peng, X. Wood-Derived Lightweight and Elastic Carbon Aerogel for Pressure Sensing and Energy Storage. *Adv. Funct. Mater.* **2020**, *30*, 1910292.

(45) Xu, S.; Li, X.; Sui, G.; Du, R.; Zhang, Q.; Fu, Q. Plasma Modification of PU Foam for Piezoresistive Sensor with High Sensitivity, Mechanical Properties and Long-Term Stability. *Chem. Eng. J.* **2020**, *381*, 122666.

(46) Guo, H.; Zhou, J.; Li, Q.; Li, Y.; Zong, W.; Zhu, J.; Xu, J.; Zhang, C.; Liu, T. Emerging Dual-Channel Transition-Metal-Oxide Quasieraerogels by Self-Embedded Templating. *Adv. Funct. Mater.* **2020**, *30*, 2000024.

(47) Wang, Y.; Shi, Z.; Yin, J. Facile Synthesis of Soluble Graphene Via a Green Reduction of Graphene Oxide in Tea Solution and Its Biocomposites. *ACS Appl. Mater. Interfaces* **2011**, *3*, 1127–1133.

(48) Thakur, S.; Karak, N. Green Reduction of Graphene Oxide by Aqueous Phytoextracts. *Carbon* **2012**, *50*, 5331–5339.

(49) Karickhoff, S. W.; Bailey, G. W. Optical Absorption Spectra of Clay Minerals. *Clays Clay Miner.* **1973**, *21*, 59–70.

(50) Huang, Z.; Guo, H.; Zhang, C. Assembly of 2D Graphene Sheets and 3D Carbon Nanospheres into Flexible Composite Electrodes for High-Performance Supercapacitors. *Compos. Commun.* **2019**, *12*, 117–122.

(51) Zong, J.; Ni, W.; Xu, H.; Ding, F.; Wang, T.; Feng, W.; Liu, X. High Tap-Density Graphene Cathode Material for Lithium-Ion Capacitors Via a Mass-Scalable Synthesis Method. *Chem. Eng. J.* **2019**, *360*, 1233–1240.

(52) Zhang, F.; Feng, Y.; Qin, M.; Gao, L.; Li, Z.; Zhao, F.; Zhang, Z.; Lv, F.; Feng, W. Stress Controllability in Thermal and Electrical Conductivity of 3D Elastic Graphene-Crosslinked Carbon Nanotube Sponge/Polyimide Nanocomposite. *Adv. Funct. Mater.* **2019**, *29*, 1901383.

(53) Zhang, F.; Feng, Y.; Qin, M.; Ji, T.; Lv, F.; Li, Z.; Gao, L.; Long, P.; Zhao, F.; Feng, W. Stress-Sensitive Thermally Conductive Elastic Nanocomposite Based on Interconnected Graphite-Welded Carbon Nanotube Sponges. *Carbon* **2019**, *145*, 378–388.

(54) Tian, J.; Yang, H.; Fu, C.; Sun, M.; Wang, L.; Liu, T. In-Situ Synthesis of Microspherical Sb@C Composite Anode with High Tap Density for Lithium/Sodium-Ion Batteries. *Compos. Commun.* **2020**, *17*, 177–181.

(55) Guo, H.; Feng, Q.; Xu, K.; Xu, J.; Zhu, J.; Zhang, C.; Liu, T. Self-Templated Conversion of Metallogel into Heterostructured TMP@Carbon Quasieraerogels Boosting Bifunctional Electrocatalysis. *Adv. Funct. Mater.* **2019**, *29*, 1903660.

(56) Wang, Y.; Chen, F.; Liu, Z.; Tang, Z.; Yang, Q.; Zhao, Y.; Du, S.; Chen, Q.; Zhi, C. A Highly Elastic and Reversibly Stretchable All-Polymer Supercapacitor. *Angew. Chem., Int. Ed.* **2019**, *58*, 15707–15711.

(57) Yu, C.; Xu, H.; Zhao, X.; Sun, Y.; Hui, Z.; Du, Z.; Sun, G.; Miao, C.; Zhou, J.; Chen, Q.; Huang, W. Scalable Preparation of High Performance Fibrous Electrodes with Bio-Inspired Compact Core-Fluffy Sheath Structure for Wearable Supercapacitors. *Carbon* **2020**, *157*, 106–112.

(58) Li, L.; Wang, K.; Huang, Z.; Zhang, C.; Liu, T. Highly Ordered Graphene Architectures by Duplicating Melamine Sponges as a Three-Dimensional Deformation-Tolerant Electrode. *Nano Res.* **2016**, *9*, 2938–2949.

(59) Li, L.; Zhang, Y.; Lu, H.; Wang, Y.; Xu, J.; Zhu, J.; Zhang, C.; Liu, T. Cryopolymerization Enables Anisotropic Polyaniline Hybrid Hydrogels with Superelasticity and Highly Deformation-Tolerant Electrochemical Energy Storage. *Nat. Commun.* **2020**, *11*, 62.

(60) Wanasekara, N. D.; Matolyak, L. E.; Korley, L. T. J. Tunable Mechanics in Electrospun Composites Via Hierarchical Organization. *ACS Appl. Mater. Interfaces* **2015**, *7*, 22970–22979.

(61) Zhao, J.; Li, J.; Li, Y.; You, J. Thermoplastic Shape Memory Composites with Enhanced Recovery Stress and Recovery Ratio Based on Double Roles of PVAc-g-GO. *Compos. Commun.* **2019**, *13*, 52–56.

(62) Xu, T.; Ding, Y.; Wang, Z.; Zhao, Y.; Wu, W.; Fong, H.; Zhu, Z. Three-Dimensional and Ultralight Sponges with Tunable Conductivity Assembled from Electrospun Nanofibers for a Highly Sensitive Tactile Pressure Sensor. *J. Mater. Chem. C* **2017**, *5*, 10288–10294.

(63) Wu, Y.-h.; Liu, H.-z.; Chen, S.; Dong, X.-c.; Wang, P.-p.; Liu, S.-q.; Lin, Y.; Wei, Y.; Liu, L. Channel Crack-Designed Gold@PU Sponge for Highly Elastic Piezoresistive Sensor with Excellent Detectability. *ACS Appl. Mater. Interfaces* **2017**, *9*, 20098–20105.

(64) Xiao, J.; Tan, Y.; Song, Y.; Zheng, Q. A Flyweight and Superelastic Graphene Aerogel as a High-Capacity Adsorbent and Highly Sensitive Pressure Sensor. *J. Mater. Chem. A* **2018**, *6*, 9074–9080.

(65) Huang, J.; Wang, J.; Yang, Z.; Yang, S. High-Performance Graphene Sponges Reinforced with Polyimide for Room-Temperature Piezoresistive Sensing. *ACS Appl. Mater. Interfaces* **2018**, *10*, 8180–8189.

(66) Zhu, C.; Han, T. Y.-J.; Duoss, E. B.; Golobic, A. M.; Kuntz, J. D.; Spadaccini, C. M.; Worsley, M. A. Highly Compressible 3D Periodic Graphene Aerogel Microlattices. *Nat. Commun.* **2015**, *6*, 6962.

(67) Cao, A.; Dickrell, P. L.; Sawyer, W. G.; Ghasemi-Nejhad, M. N.; Ajayan, P. M. Super-Compressible Foamlike Carbon Nanotube Films. *Science* **2005**, *310*, 1307–1310.

(68) Liang, H.-W.; Guan, Q.-F.; Chen, L.-F.; Zhu, Z.; Zhang, W.-J.; Yu, S.-H. Macroscopic-Scale Template Synthesis of Robust Carbonaceous Nanofiber Hydrogels and Aerogels and Their Applications. *Angew. Chem., Int. Ed.* **2012**, *51*, 5101–5105.

(69) Gui, X.; Wei, J.; Wang, K.; Cao, A.; Zhu, H.; Jia, Y.; Shu, Q.; Wu, D. Carbon Nanotube Sponges. *Adv. Mater.* **2010**, *22*, 617–621.

(70) Wang, D.; Song, J.; Lin, S.; Wen, J.; Ma, C.; Yuan, Y.; Lei, M.; Wang, X.; Wang, N.; Wu, H. A Marine-Inspired Hybrid Sponge for Highly Efficient Uranium Extraction from Seawater. *Adv. Funct. Mater.* **2019**, *29*, 1901009.

(71) Dong, X.; Wei, Y.; Chen, S.; Lin, Y.; Liu, L.; Li, J. A Linear and Large-Range Pressure Sensor Based on a Graphene/Silver Nanowires Nanobiocomposites Network and a Hierarchical Structural Sponge. *Compos. Sci. Technol.* **2018**, *155*, 108–116.

(72) Ding, Y.; Yang, J.; Tolle, C. R.; Zhu, Z. Flexible and Compressible PEDOT:PSS@Melamine Conductive Sponge Prepared Via One-Step Dip Coating as Piezoresistive Pressure Sensor for Human Motion Detection. *ACS Appl. Mater. Interfaces* **2018**, *10*, 16077–16086.

(73) Ma, Z.; Wei, A.; Ma, J.; Shao, L.; Jiang, H.; Dong, D.; Ji, Z.; Wang, Q.; Kang, S. Lightweight, Compressible and Electrically Conductive Polyurethane Sponges Coated with Synergistic Multiwalled Carbon Nanotubes and Graphene for Piezoresistive Sensors. *Nanoscale* **2018**, *10*, 7116–7126.

(74) Wang, H.; Lu, W.; Di, J.; Li, D.; Zhang, X.; Li, M.; Zhang, Z.; Zheng, L.; Li, Q. Ultra-Lightweight and Highly Adaptive All-Carbon Elastic Conductors with Stable Electrical Resistance. *Adv. Funct. Mater.* **2017**, *27*, 1606220.

(75) Lu, Y.; He, W.; Cao, T.; Guo, H.; Zhang, Y.; Li, Q.; Shao, Z.; Cui, Y.; Zhang, X. Elastic, Conductive, Polymeric Hydrogels and Sponges. *Sci. Rep.* **2014**, *4*, 5792.

(76) Cai, Y.; Shen, J.; Dai, Z.; Zang, X.; Dong, Q.; Guan, G.; Li, L.-J.; Huang, W.; Dong, X. Extraordinarily Stretchable All-Carbon Collaborative Nanoarchitectures for Epidermal Sensors. *Adv. Mater.* **2017**, *29*, 1606411.

(77) Yu, X.-G.; Li, Y.-Q.; Zhu, W.-B.; Huang, P.; Wang, T.-T.; Hu, N.; Fu, S.-Y. A Wearable Strain Sensor Based on a Carbonized Nano-Sponge/Silicone Composite for Human Motion Detection. *Nanoscale* **2017**, *9*, 6680–6685.

(78) Huang, W.; Dai, K.; Zhai, Y.; Liu, H.; Zhan, P.; Gao, J.; Zheng, G.; Liu, C.; Shen, C. Flexible and Lightweight Pressure Sensor Based on Carbon Nanotube/Thermoplastic Polyurethane-Aligned Conductive Foam with Superior Compressibility and Stability. *ACS Appl. Mater. Interfaces* **2017**, *9*, 42266–42277.

(79) Iglío, R.; Mariani, S.; Robbiano, V.; Strambini, L.; Barillaro, G. Flexible Polydimethylsiloxane Foams Decorated with Multiwalled Carbon Nanotubes Enable Unprecedented Detection of Ultralow Strain and Pressure Coupled with a Large Working Range. *ACS Appl. Mater. Interfaces* **2018**, *10*, 13877–13885.

(80) Wang, Y.; Tebyetekerwa, M.; Liu, Y.; Wang, M.; Zhu, J.; Xu, J.; Zhang, C.; Liu, T. Extremely Stretchable and Healable Ionic Conductive Hydrogels Fabricated by Surface Competitive Coordination for Human-Motion Detection. *Chem. Eng. J.* **2020**, DOI: 10.1016/j.cej.2020.127637.

(81) Trung, T. Q.; Hoang Sinh, L.; Thi My Linh, D.; Ju, S.; Park, S. Y.; Lee, N.-E. Freestanding, Fiber-Based, Wearable Temperature Sensor with Tunable Thermal Index for Healthcare Monitoring. *Adv. Healthcare Mater.* **2018**, *7*, No. e1800074.

(82) Xu, X.; Zhang, Q.; Hao, M.; Hu, Y.; Lin, Z.; Peng, L.; Wang, T.; Ren, X.; Wang, C.; Zhao, Z.; Wan, C.; Fei, H.; Wang, L.; Zhu, J.; Sun, H.; Chen, W.; Du, T.; Deng, B.; Cheng, G. J.; Shakir, I.; Dames, C.; Fisher, T. S.; Zhang, X.; Li, H.; Huang, Y.; Duan, X. Double-Negative-Index Ceramic Aerogels for Thermal Superinsulation. *Science* **2019**, *363*, 723–727.

(83) Si, Y.; Wang, X.; Dou, L.; Yu, J.; Ding, B. Ultralight and Fire-Resistant Ceramic Nanofibrous Aerogels with Temperature-Invariant Superelasticity. *Sci. Adv.* **2018**, *4*, No. eaas8925.

(84) Zhang, S.; Feng, J.; Feng, J.; Jiang, Y.; Li, L. Ultra-Low Shrinkage Chitosan Aerogels Trussed with Polyvinyl Alcohol. *Mater. Des.* **2018**, *156*, 398–406.

(85) Kobayashi, Y.; Saito, T.; Isogai, A. Aerogels with 3D Ordered Nanofiber Skeletons of Liquid-Crystalline Nanocellulose Derivatives as Tough and Transparent Insulators. *Angew. Chem., Int. Ed.* **2014**, *53*, 10394–10397.

■ NOTE ADDED AFTER ASAP PUBLICATION

This article originally published with errors in Figure 6. The corrected Figure 6 published February 5, 2021.